Journal of Non-Crystalline Solids 666 (2025) 123710

Contents lists available at ScienceDirect

Journal of Non-Crystalline Solids

journal homepage: www.elsevier.com/locate/jnoncrysol

Doping ZnO in low boron calcium borosilicate glass-ceramics for high-performance dielectric LTCC substrate

Kaiyu Huang [a], Chaofan Wang [a], Maoyuan Yang [a], Qingchao Jia [a], Wenzhi Wang [a], Chen Chen [b], Huidan Zeng [a,*], Xiongke Luo [b,*]

[a] School of Materials Science and Engineering, East China University of Science and Technology, Shanghai 200237, China
[b] Shanghai Zenfocus Semiconductor Technology Co., Ltd., Shanghai 201206, China

ARTICLE INFO

Keywords:
Glass-ceramics
$CaO-B_2O_3-SiO_2$
β-$CaSiO_3$
ZnO

ABSTRACT

$CaO-B_2O_3-SiO_2$ (CBS) glass-ceramics is one of the most widely used commercial low-temperature co-fired ceramic (LTCC) substrate materials due to its excellent dielectric and mechanical properties. However, medium-high boron CBS glass suffers from challenge such as difficulty in melting, volatility and phase separation, leading to its inability to balance the competition between sintering and crystallization. The introduction of ZnO to replace part of the B_2O_3 may be able to solve the above problems effectively. Specifically, the networks modifier ZnO can be used to reduce sintering temperatures by decreasing network aggregation in the glass. Our study found that the higher the content of ZnO, the more non-bridging oxygen in the glass network, the lower the temperature at which glass-ceramics can be sintered densified. With 4 mol % ZnO, the glass-ceramics can be densified at 850 °C with a dielectric constant of 5.29 and a dielectric loss of 3.12×10^{-4} at 1 MHz and a bending strength of 174 MPa. This work presents a novel idea for the design of advanced glass-ceramics.

1. Introduction

The rapid evolution of microwave communication technology demands substrates with lower dielectric constants and minimized dielectric loss to decrease coupling losses [1], boost signal transmission rates, and enhance frequency selectivity [2]. Commonly used substrates include ceramics [3–6], glass ceramic composite systems [7–9], and glass-ceramics systems [10–12]. Glass-ceramics are considered as potential LTCC materials because of their ability to be sintered at lower temperatures and their excellent dielectric and mechanical properties [13–14]. Due to the low dielectric constant of 5 and the low loss of about 2.0×10^{-4} of $CaSiO_3$ [15], $CaO-B_2O_3-SiO_2$ (CBS) glass-ceramics with wollastonite as the main crystalline phase have been widely studied [16–17] and have been applied in Ferro A6M [18]. Contemporary studies on CBS systems often highlight a higher boron content [19–21], allowing the glass to enhance sinterability at reduced temperatures. Nonetheless, heightened boron levels lead to mismatches between $[BO_3]$ and $[SiO_4]$ units, exacerbating phase separation and component enrichment [22], which manifest as stable, immiscible opacities [23]. These difficulties emphasize the advantages of low-boron CBS glass-ceramics. However, it is a challenge to balance sintering and crystallization and make it able to be sintered densified at a low temperature (<870 °C) [22–24].

External ions such as alkali and alkaline earth metals are commonly used as sintering aids to cope with these challenges [25–26]. In this way, network connectivity is reduced and short-range structural interactions within the glass are altered to achieve good densification. While additives like K_2O have traditionally been used to induce more liquid phase during sintering, their polarization effects inadvertently raise the dielectric constant [27]. Similarly, Li_2O and Na_2O can disrupt network connectivity but at the cost of structural defects and increased ionic conductivity, degrading overall dielectric properties [28]. Additionally, MgO increases the non-bridging oxygen content but its high field strength excessively stabilizes the glass network, dampening its fluxing effectiveness [29]. Some studies have shown that doping ZnO as a flux can effectively balance sintering and crystallization [30].

We have achieved enhancement of sintering ability by reducing the degree of glass network polymerization. The presence of ZnO disrupts $[BO_4]$ and $[SiO_4]$ units, leading to the formation of a large number of non-bridging oxygen atoms, which results in a decrease in the glass transition temperature and crystallization temperature, and makes the liquid phase occur at a lower temperature. The appropriate ZnO content

* Corresponding authors.
E-mail addresses: hdzeng@ecust.edu.cn (H. Zeng), jackie_luo@zenfocuscorp.com (X. Luo).

https://doi.org/10.1016/j.jnoncrysol.2025.123710
Received 28 April 2025; Received in revised form 13 July 2025; Accepted 14 July 2025
Available online 21 July 2025

not only refines the sintering performance of the glass-ceramics but also improves their mechanical strength. Moreover, its role as a network modifier breaks the Si-O-Si bond, which facilitates the precipitation of α-SiO_2 (ε_r − 4) [31] and maintains a low dielectric constant. Our work provides a new strategy for enhancing sintering performance while maintaining dielectric properties of glass-ceramics.

2. Materials and methods

2.1. Preparation of ZCBS glass-ceramics

The CBS glass was fabricated by melt quenching method using $CaCO_3$, H_3BO_3, SiO_2 and ZnO reagents as raw materials. In this experiment, a low boron system with CaO/SiO_2 ratio of 0.8 and 5 mol % B_2O_3 was used, and different amounts of ZnO (0–6 mol %) were added to the parent glass. The samples of glass-ceramics were labeled Z0, Z2, Z4, and Z6, respectively. The stoichiometric moles of glass formulations are shown in Table 1. The corresponding raw materials were accurately weighed according to the composition, mixed with 5 wt % deionized water and polytetrafluoroethylene, and pressed into round cakes with a diameter of 3 cm. The platinum crucible was heated in a high-temperature lifting furnace, fed at 1400 °C, and kept at 1500 °C for 3 h to fully melt. The molten glass was then poured into deionized water to quench and prevent crystallization. After water quenching, the glass was dried, ground with an agate mortar, and passed through a 40-mesh screen. After two-step ball milling, fine glass powder was obtained, and DTA and infrared tests were carried out. The rest of the glass powder was mixed with a PVA binder in proportion, placed into a mold, pressed and formed at 20 MPa, and sintered to obtain glass-ceramics. The specific heat treatment process is shown in Fig. S1. The density, crystal phase composition, thermal expansion and dielectric properties of the glass-ceramics were then tested.

2.2. Characterization

The actual post-melting glass composition was characterized by inductively coupled plasma (ICP, PerkinElmer ICP 2100) analysis. Infrared spectral images of sintered samples were obtained using a Fourier transform infrared spectrometer (FTIR, IR Affinity-1, Shimadzu, Japan) with a scanning range of 400–1800 cm^{-1}. Boron coordination environments were characterized by ^{11}B solid-state nuclear magnetic resonance (NMR). Experiments were carried out on a Bruker Avance III HD 500 M spectrometer (11.7 T). The resonance frequency for ^{11}B is 160.46 MHz. All the spectra were recorded using a 4-mm Bruker magic angle spinning (MAS) probe. ^{11}B MAS spectra were obtained at a spinning speed of 10 kHz. The pulse length is 0.81 μs (15° liquid angle) with a recycle delay of 64 s. Chemical shifts were referenced to 1 M H_3BO_3 (=19.4 ppm). The binding energies of Zn and O in the samples were analyzed by X-ray photoelectron spectroscopy (XPS, Thermo Scientific K-Alpha). Crystallization kinetics were analyzed using a differential thermal analyzer (DTA, HCT-3, Beijing Hengjiu). Approximately 19 mg of the sample was examined from room temperature to 1000 °C in an air atmosphere, with Al_2O_3 as the reference sample. Heating rates of 10 °C/min were employed. XRD pattens were obtained by scanning at 10–80 ° using an X-ray diffractometer (18 KW, D\max 2550 VB, PC, Rigaku, Japan), and Jade was used to analyze the information on the phases and volume fraction of phases in the XRD pattens, and was used to analyze the relative content of each phase in the XRD pattens. Sintering images and shrinkage were tested on samples with a diameter of about 4 mm using an image sintering point tester (SSY-1700, Xiangtan Instrument Co., Ltd.). Apparent porosity (δ), water absorption (μ), and bulk density (ρ) of the samples were determined using the boiling method specified in the national standard GB/T 3810.1–2006. The calculation formulas are given in Eqs. (1–3):

$$\delta = \frac{M_3 - M_1}{M_3 - M_2} \times 100\% \tag{1}$$

$$\mu = \frac{M_3 - M_1}{M_1} \times 100\% \tag{2}$$

$$\rho = \frac{M_1}{M_3 - M_2} \times D_l \tag{3}$$

where M_1 is the mass of the dried sample in air, M_2 is the mass of the saturated sample in water, M_3 is the mass of the saturated sample in air, and D_l is the density of the liquid at the experimental temperature. In this study, the density of water is considered to be 0.998 g/cm^3. Field emission scanning electron microscopy (SEM, Hitachi High-Technologies, Japan) was used to analyze the crystalline morphology of the samples with the growth process of precipitated crystals. Dielectric constant and dielectric loss of the disc sintered samples were tested at 1 MHz frequency using a broadband dielectric impedance spectrometer (Concept 40, NOVOCONTROL, Germany). Three-point flexural strength experiments were performed on strip sintered samples using a universal testing machine (30 kN 0.005–500 mm/min/3367, Instron, USA) according to the international standard GB/T 38,978–2020. The thermal expansion curve was tested at a heating rate of 5 K/min using a dilatometer (DIL-III, China). The formula for calculating the coefficient of thermal expansion is shown in Eq. (4):

$$\alpha = \frac{\Delta L}{\Delta T \times L_0} \tag{4}$$

where α is the coefficient of thermal expansion, the unit is K^{-1}; ΔL is the length change of the sample during the test, in mm; ΔT is the temperature change, expressed in K; L_0 is the initial length of the sample, expressed in mm.

Table 1
ZCBS glass formulation and state of the glass after water quenching.

Sample	CaO	B_2O_3	SiO_2	ZnO	Condition of glass
Z0	43.14	5.07	51.78	0.00	Transparent
Z2	42.28	4.97	50.75	2.00	Transparent
Z4	40.59	4.87	49.73	4.00	Transparent
Z6	38.15	4.77	48.74	6.00	Transparent

3. Result and discussion

3.1. Effect of ZnO content on the structure of CBS glass

To verify compositional consistency between designed and as-melted glasses, inductively coupled plasma (ICP) analysis was performed followed by oxide content normalization. Weight percentages of constituent oxides in nominal and actual compositions are detailed in Tables S1 and S2, respectively. The results demonstrate effective ZnO incorporation into the glass network, while reduced B_2O_3 content minimized volatilization losses. The marginal CaO deficit likely resulted from powder entrainment during CO_2 liberation in carbonate decomposition. Overall, no significant deviation exists between designed and actual compositions. To confirm the amorphous nature of the water-quenched samples, X-ray diffraction (XRD) analysis was performed on crushed powders, as shown in Fig. S2. The XRD patterns reveal broad diffuse halos, characteristic of amorphous materials, for all four compositions. This absence of sharp crystalline diffraction peaks confirms that the water-quenched samples retained their amorphous state. In order to study the effect of ZnO content on the structure of CBS glass, Fig. 1(a) shows the FT-IR spectra of ZCBS glass in the range of 400–1600 cm^{-1}, illustrating that the doping of ZnO has a significant effect on the CBS glass, as can be seen from the change in peak strength. Peaks around 1451 cm^{-1}, 1044 cm^{-1}, 907 cm^{-1}, 731 cm^{-1}, 517 cm^{-1}, and 455 cm^{-1} are observed. The absorption peak at 455 cm^{-1} corresponds to the

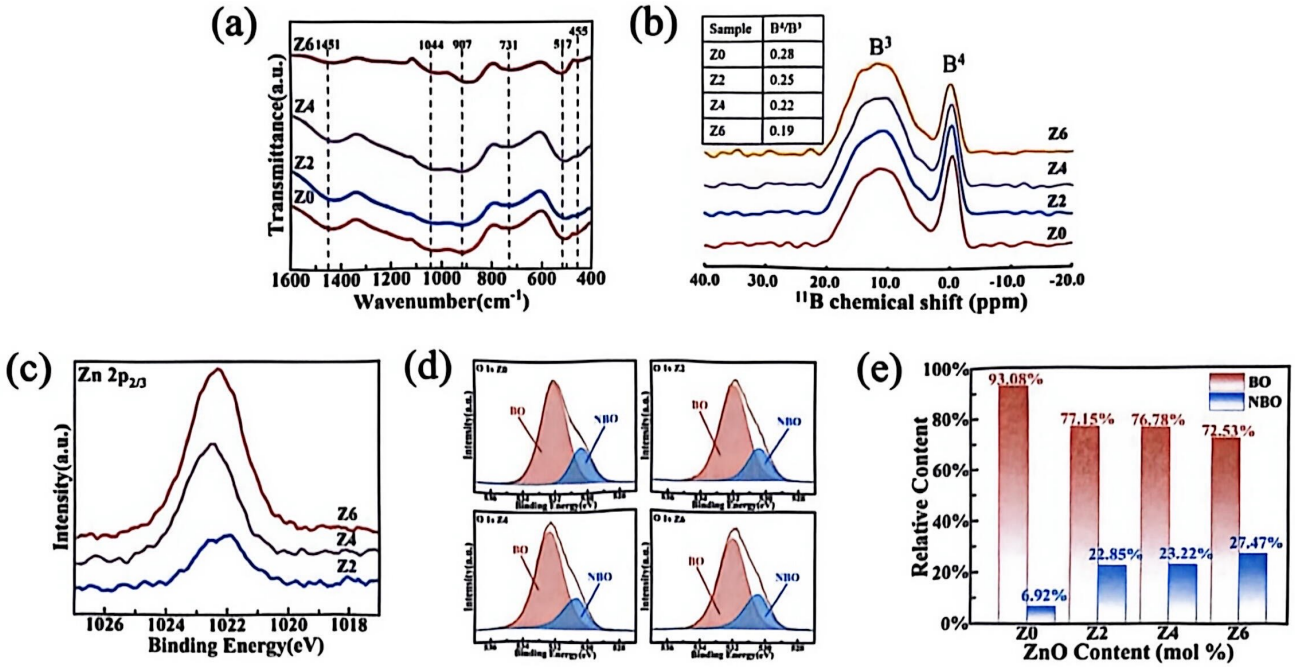

Fig. 1. Structural properties of the ZCBS glass. (a) The FT-IR spectra of ZCBS glass; (b) The ^{11}B solid-state NMR spectrum of ZCBS glass; (c) The Zn $2p_{2/3}$ XPS spectra of ZCBS glass; (d) The de-coiling integral peak of O 1 s XPS for Z0,Z2,Z4,Z6; (e) The relative content of BO—NBO calculated according to the fitting peak.

antisymmetric deformation vibration of $[SiO_4]$. The absorption peak at 517 cm^{-1} can be attributed to the vibration of metal cations Ca^{2+} and Zn^{2+} [32] and the deformation mode of the Si-O single bond in the network [33]. The absorption peak at the 731 cm^{-1} position is generally attributed to the B-O-B connection between two $[BO_3]$ units [34]. The absorption peak at 907 cm^{-1} is classified as Si-NBO in $[SiO_4]$ [35]. The absorption peak at 1044 cm^{-1} corresponds to B-O in $[BO_4]$ [33]. The absorption peak at 1451 cm^{-1} is attributed to the asymmetric tensile vibration of the $[BO_3]$ unit. As can be seen from Fig. 1(a), with the increase of ZnO introduced, the peaks of 1044 cm^{-1} corresponding to the $[BO_4]$ unit weaken and the peaks at 731 cm^{-1} and 1451 cm^{-1} corresponding to $[BO_3]$ are enhanced, which means that $[BO_4]$ is transformed into $[BO_3]$ in the glass network structure. The 907 cm^{-1} peak corresponding to Si-NBO is enhanced, indicating that the amount of non-bridging oxygen in the glass network increases, which is proof that Zn^{2+} plays a role in breaking the network in the CBS glass and means that the stability of the glass network structure is weakened. The distribution of FT-IR spectral bands is shown in Table 2. To more clearly and intuitively characterize the boron coordination environment in the glass, we performed ^{11}B solid-state nuclear magnetic resonance (NMR) spectroscopy, with the results presented in Fig. 1(b). Analysis of the spectra reveals that as the ZnO doping level increases, the $[BO_4]/[BO_3]$ ratio gradually decreases, indicating a conversion of $[BO_4]$ to $[BO_3]$ units. This finding is in agreement with the FTIR results. Zn^{2+} ion, as a network intermediate, can form $[ZnO_4]$ units to promote the formation of the glass network, and can also play a role in compensating charge outside the network structure [36–37]. In order to study the role of Zn^{2+} in the glass network structure, Fig. 1(c) shows the Zn $2p_{2/3}$ XPS spectrum of ZCBS glass. The increase in peak intensity and peak area proves the increase in the amount of Zn^{2+}. The results show that the peak of Zn^{2+} is basically unchanged and concentrated in 1022 (eV), which is consistent with the situation reported in the paper [38] indicating that Zn^{2+} mainly exists as a network modifier, and the role as a network modifier of Zn^{2+} in the experiment did not change within the doping amount range of 0–6 mol %. In order to analyze the effect of ZnO doping amount on the amount of bridging oxygen (BO) and non-bridging oxygen (NBO) in the glass network structure, the de-coiling integral peak of O 1 s XPS for each glass structure is shown in Fig. 1(c). As can be seen from Fig. 1(d), with the increase of ZnO, the peak strength and peak area representing BO in the glass structure decrease, while the peak strength and peak area representing NBO in the glass structure increase, which indicates that the amount of NBO in the glass structure increases at the expense of the decrease of the amount of BO. In order to more intuitively see the relative content changes of BO and NBO in the glass network structure, the fitted peak area was calculated to quantitatively analyze the ratio of bridging oxygen to non-bridging oxygen in the glass network. The results are shown in Fig. 1(e). When ZnO is not doped, the relative content of BO in the CBS glass network is 93.08 %. When ZnO is added with 2 mol %, the relative content of BO rapidly decreases to 77.15 %, and then continuously decreases to 72.53 % when ZnO is added with 6 mol %, while the relative content of NBO increases from 6.92 % of Z0 to 27.47 % of Z6, which proves the obvious disconnection effect of Zn^{2+}. At the same time, it means that the peak value of BO moves to the direction of lower energy, corresponding to the broken bond of Si-O-Si in FT-IR and the BO of high binding energy decreases.

Table 2
Allocation of FT-IR spectral bands.

Wavenumber/cm^{-1}	Main vibration types
455	the antisymmetric deformation vibration of $[SiO_4]$
517	Si-O-Si and the vibration of Ca^{2+} and Zn^{2+}
731	B-O-B between two $[BO_3]$ units
907	Si-NBO in $[SiO_4]$
1044	B-O in $[BO_4]$
1451	the asymmetric tensile vibration of $[BO_3]$

3.2. Effect of ZnO content on sintering and crystallization of ZCBS glass-ceramics

Since the particle size of the glass powder is closely related to its sintering performance, it's necessary to determine the particle size distribution of each glass powder composition. Fig. S3 shows that the median particle size(D_{50}) of the glass powders is approximately 1.5 μm. To evaluate the effect of ZnO introduction on the thermal properties of

the glass, Fig. 2(a) compares the DTA curves of ZCBS glass with different doping amounts of ZnO. The heat absorption peak observed in the figure, that is, the temperature corresponding to the intersection point of the downward step tangent, is the glass transition temperature (T_g); the heat release peak observed corresponds to the process of crystallization behavior of glass-ceramics during heating; the temperature corresponding to the highest peak is the crystallization peak temperature (T_p); the initial temperature of the crystallization peak corresponds to the initial temperature of crystallization (T_x). The DTA results show that the addition of 4 mol % ZnO reduces T_g from 685 °C to 677 °C, T_x from 817 °C to 801 °C, T_p from 843 °C to 826 °C, and the characteristic temperature decreases continuously with the further increase of ZnO. At the same time, the simultaneous decrease in crystallization peak height accompanied by peak broadening suggests potential precipitation of a secondary crystalline phase within the system. This trend aligns with DTA observations reported by Jia [16] for CBS glass-ceramics, where closely spaced crystallization exotherms arising from dual phases resulted in significantly diminished peak intensities. The difference between T_x and T_g ($\Delta T = T_x - T_g$) is used to characterize the thermal stability of glass [39], the larger the ΔT, the better the thermal stability of the glass. After calculating the difference, it is found that the addition of ZnO makes the ΔT of CBS glass tend to decrease, and the thermal stability of the glass decreases. In combination with the result of FT-IR, it is mainly due to the conversion of frame [BO_4] to layer [BO_3] and the addition of Zn^{2+} breaking the Si-O-Si bond between [SiO_4] cells, resulting in the loose structure of the glass network. The specific

Table 3
Characteristic temperature value of ZCBS glass.

Sample	Glass transition temperature T_g(°C)	Initiation temperature of crystallization T_x(°C)	ΔT T_x-T_g(°C)	Peak temperature of crystallization T_p(°C)
Z0	685	817	132	843
Z2	684	808	124	830
Z4	677	801	124	826
Z6	669	786	117	806

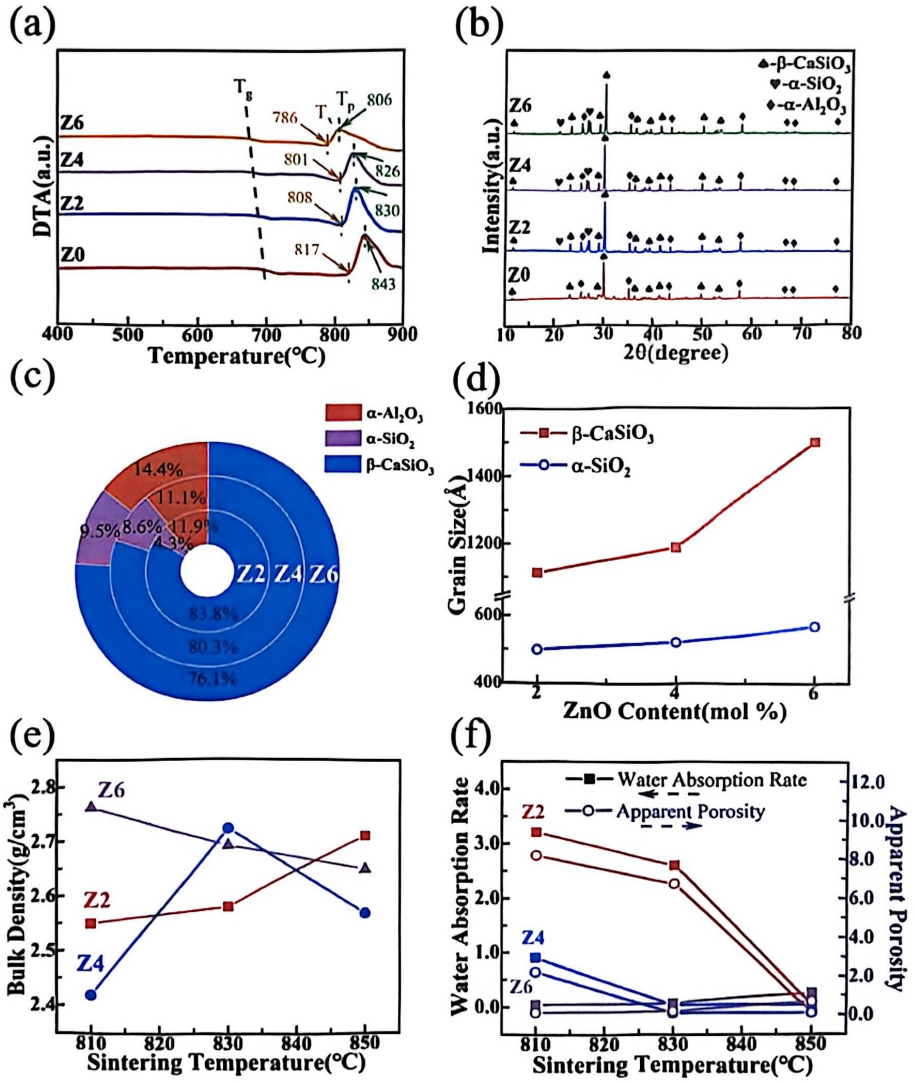

Fig. 2. Crystallization and sintering properties of the ZCBS glass-ceramics. (a) The DTA curves of ZCBS glass; (b) The XRD patterns of Z0-Z6 sintered at 850 °C; (c) The proportion of each crystal phase analyzed by semi-quantitative analysis with XRD; (d) The grain size obtained by XRD refinement; (e) Water absorption and porosity of Z2, Z4 and Z6 sintered at 810 °C, 830 °C and 850 °C, respectively; (f) The bulk density of Z2, Z4 and Z6 sintered at 810 °C, 830 °C and 850 °C, respectively.

characteristic temperature values are summarized in Table 3. DTA shows that the increase of ZnO content can affect the crystallization behavior of the CBS glass-ceramics, then XRD is used to investigate the change of crystallization. The glass powder was held at 850 °C for 20 min and sintered, XRD test was conducted, and subsequent semi-quantitative analysis was conducted with 10 wt % α-Al_2O_3 as the internal standard, as shown in Fig. 2(b)-(d). Fig. 2(b) XRD qualitative analysis shows that only β-$CaSiO_3$ (PDF ID:04–010–2581) was precipitated by Z0, while the precipitation of α-SiO_2 (PDF ID:03–065–0466) can be observed in samples with ZnO at $2\theta = 26°$. This change may be due to the breaking of the Si-O-Si bond between [SiO_4] units by Zn^{2+}, making [SiO_4] shift from a state of high polymerization to a state of low polymerization, which is beneficial to the precipitation of α-SiO_2. ZnO was doped in the parent glass, but no crystal phase related to Zn was precipitated, indicating that Zn elements were all distributed in the glass phase and did not participate in crystallization. In order to show the degree of crystallization weakening more directly, Rietveld refinement was used to conduct semi-quantitative XRD analysis, and the fitting result $R/E < 1.5$, the proportion of each crystal and the fitting grain size are shown in Fig. 2(c)(d). Fig. 2(c) shows the content of each crystal phase in the sample. It is found that with the increase of ZnO content, the proportion of α-Al_2O_3 in the crystal increases, corresponding to the decrease of the content of other crystal phases in the sample, indicating that the overall crystallization degree is weakened. After conversion, the content of each part of the crystal phase in the glass-ceramics is shown in Table 4. After calculation, it is found that when the ZnO introduced amount increases from 2 mol % to 6 mol %, the β-$CaSiO_3$ crystal precipitation decreases from 70.42 wt % to 52.85 wt %, and the α-SiO_2 crystal precipitation increases from 3.61 wt % to 6.60 wt %, indicating that there is a competitive relationship between the two. The introduction of ZnO can improve the precipitation capacity of α-SiO_2, which may due to Zn^{2+} breaking part of the Si-O-Si bond between [SiO_4] units. Moreover, the content of glass phase is greatly increased, which proves the excellent melting effect of ZnO. Fig. 2(d) shows the grain size changes of each crystal. With the increase of ZnO content, β-$CaSiO_3$ grains grow larger, indicating that its nucleation ability decreases. On the contrary, α-SiO_2 grain growth trend is slow, indicating that the introduction of ZnO mainly promotes its nucleation ability [40]. Sintering image analysis was conducted on all four glass powder compositions to determine their softening behavior and the results are presented in Fig. S4. The images reveal that both the onset temperature of shrinkage and shrinkage completion temperature decrease progressively with increasing ZnO content. The initiation of shrinkage in glass-ceramics signifies the formation of a liquid phase and the commencement of viscous flow. The observed reduction in softening point indicates that the temperature required to achieve a given viscosity decreases. Upon reaching 1000 °C, samples with higher ZnO content exhibited progressively spheroidized morphologies, indicating enhanced viscous flow behavior due to increased liquid phase formation. This demonstrates ZnO's role as a network modifier within the glass structure. The sintered density of glass-ceramics sintered at 850 °C was tested by the boiling method. The measured water absorption, apparent porosity and bulk density were shown in Fig. 2(e)(f). All the measured results are summarized in Table 5. The sample name was glass powder + sintering temperature, for example, Z2–810 was Z2 sample held at 810 °C for 20 min. When Z0 is held at 850 °C for 20 min, the measured water absorption rate is 22.24 % and the apparent porosity is 36.36 %, indicating that Z0 without doped ZnO cannot be sintered densely at 850 °C, and there are a lot of holes inside. After the introduction of 2 mol % ZnO, held at 850 °C for 20 min, the water absorption rate is reduced to 0.05 %, and the apparent porosity is reduced to 0.13 %, which means the parent glass can be sintered densely after the introduction of ZnO, as Zn^{2+} acts as a network modifier, making the network structure easier to be disrupted, increasing the liquid phase to fill the pores. Moreover, with the increase of ZnO content, the sintering temperature decreases significantly, and the water absorption of Z6 sintered at 810 °C can reach 0.04 %, which indicates that ZnO has excellent melting effect. After the introduction of ZnO, the bulk density of sintered samples can reach >2.5 g/cm^3, reflecting good sintering density [41]. However, the boiling water method cannot characterize internal porosity. To address this limitation, polished cross-sections were examined via scanning electron microscopy (SEM), and porosity was quantified using ImageJ software. Representative micrographs are presented in Fig. S5. The resulting porosity distribution trends corroborate the apparent porosity variations observed previously.

Table 4
The mass percentage of each part in glass-ceramics.

Sample	β-$CaSiO_3$	α-SiO_2	α-Al_2O_3	amorphous phase
Z2	70.42	3.61	10.00	15.97
Z4	72.34	7.75	10.00	9.91
Z6	52.85	6.60	10.00	30.55

Table 5
Summary of sintered density of glass-ceramics measured by boiling method.

Sample - sintering temperature	Water absorption rate (%)	Apparent porosity (%)	Bulk density (g/cm^3)
Z0–850	22.24	36.36	1.63
Z2–810	3.21	8.19	2.55
Z2–830	2.58	6.68	2.58
Z2–850	0.05	0.13	2.71
Z4–810	0.90	2.19	2.42
Z4–830	0.04	0.10	2.72
Z4–850	0.04	0.09	2.57
Z6–810	0.04	0.12	2.76
Z6–830	0.07	0.19	2.69
Z6–850	0.26	0.68	2.65

In order to observe the sintering inside the glass-ceramics, the microscopic morphology of the glass-ceramics cross-section was observed by SEM, as shown in Fig. 3(a)-(l). It can be seen from Fig. 3(a) that there are still many unsintered glass particles in the Z0–850 sample, which is because it cannot produce enough liquid phase before crystallization. Crystallization and liquid phase generation in the sintering process are competitive, and the presence of crystal particles will increase the viscosity of the liquid phase, resulting in higher difficulty in mass transfer, thus hindering the sintering process. Fig. 3(b)-(d) shows the cross-section of Z2 sintered at different temperatures, which is amplified by 80 times. It can be seen that there are basically no large pores, even Z2–810 (sample Z2 sintered at 810 °C) with an apparent porosity of 8.19 % has no obvious large pores. Fig. 3(b)-(d) shows the cross-section of Z2-Z6 sintered at 850 °C, which is amplified by 80 times. Dense sintering is shown, corresponding to the low apparent porosity and high bulk density. This should be because the network connectivity becomes worse after the addition of ZnO, and it is easier to produce liquid phases, which can fill the large pores that are already present. As shown in Fig. 3(g)-(i), the cross-section microstructure amplified by 3.0 K times after sintering of glass-ceramics can be seen to show the size and shape of crystal particles. As can be seen from Fig. 3(g), the glass particles of Z2–850 are basically melted, and the grains are small and flaky with a little overlap, with small holes, which should be due to insufficient glass phase, unable to fill the pores caused by the loss of organic matter and glass crystallization during the sintering process. In Fig. 3(h), Z4–850 has fewer pores and the holes are basically filled, which shows great sintering density. Besides, the grain size of Z4 is slightly larger than Z2, which is buried in the glass phase. As can be seen from Fig. 3(l), the crystal particle size of Z6–850 is larger, and the crystal particle is covered by the glass phase. As the glass phase cannot completely fill the gap left by the growth of the crystal particle, there are small holes. The combination of sintered crystal particles and glass phase can be seen at a magnification of 15.0 K, as shown in Fig. 3(j)-(l). In the figure, the crystal particles of the Z2–850 sample are relatively small, not fully

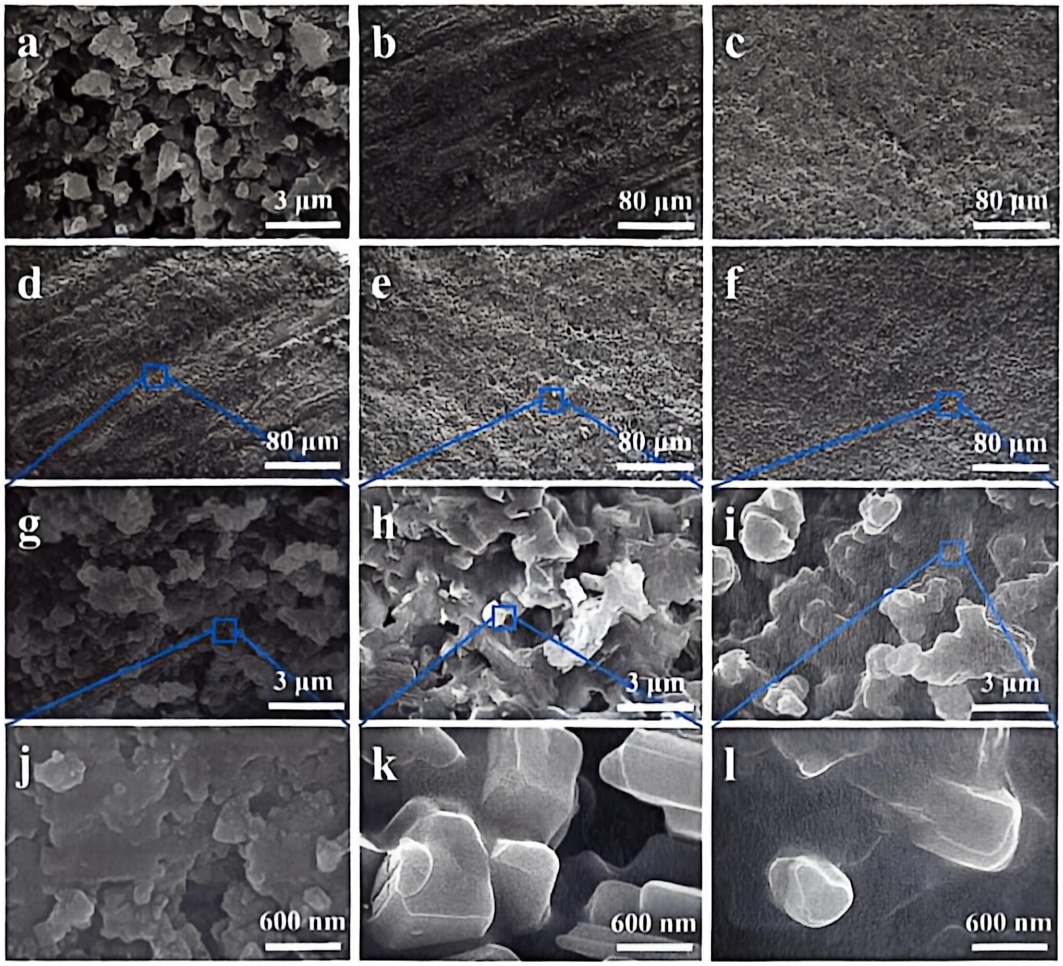

Fig. 3. The cross-section of ZCBS glass powder sintered glass-ceramic through SEM; (a)Z0–850(× 3.0 K); (b)Z2–810(× 80); (c)Z2–830(× 80); (d)Z2–850(× 80); (e) Z4–850(× 80); (f)Z6–850(× 80); (g)Z2–850(× 3.0 K); (h)Z4–850(× 3.0 K); (i)Z6–850(× 3.0 K); (j)Z2–850(× 15.0 K); (k)Z4–850(× 15.0 K); (l)Z6–850(× 15.0 K).

grown, and basically covered by the glass phase. In the Z4–850 sample, columnar β-$CaSiO_3$ crystal particles can be clearly seen, which are closely combined with glass, enhancing the strength of glass-ceramics. In Z6–850, many molten glass phases can be clearly seen, with obvious liquid phase characteristics, consistent with the results of XRD refinement. The precipitated crystals aggregate into distinct clusters, with the formation of new columnar crystals clearly observable. The particle size of the crystals exhibits a progressive increase, primarily attributed to the varying viscosity of the liquid phase during the sintering process. A lower viscosity of the liquid phase facilitates molecular transport and thereby enhances grain growth.

3.3. Properties of ZCBS glass-ceramics

The 100 °C-400 °C thermal expansion curve of 850 °C sintered glass-ceramics is shown in Fig. 4(a). According to the linear fitting of the curve, the thermal expansion coefficient in the 100 °C-400 °C temperature range is summarized in Table 6. The results show that the thermal expansion coefficient of glass-ceramics increases with the increase of ZnO introduced into the glass. This is because more glass phase will remain in the sintering process. The glass phase has an amorphous structure, and the position of its atoms is long-range disordered. This disordered structure makes the thermal expansion coefficient of the glass phase larger and shows discontinuity during heating. In terms of the bending strength of glass-ceramics, the bending strength of Z2 is low, mainly because there are many internal pores. As seen from the SEM cross-section, the grain size is too small to effectively produce adhesion. The columnar grains in Z4 sample are well combined with the glass, the pores are fewest, and the bending strength is highest. There is a gap left by crystal growth in the Z6 sample, and its crystal particle size is large, extending from the glass phase, and micro-cracks extend along the interface between the crystal and the glass phase during stress, resulting in average bending strength. The dielectric properties of glass-ceramics Z2-Z4 are shown in Fig. 4(c). The reduction in dielectric constant and loss tangent for samples from Z2 to Z4 is attributed to the increased presence of the low-dielectric-phase α-SiO_2 ($\varepsilon_r \approx 4$) and enhanced crystallinity. The decrease in dielectric constant for samples from Z4 to Z6 may be primarily attributed to the continuous increase of the α-SiO_2 crystalline phase, which exhibits a lower dielectric constant than β-$CaSiO_3$. Concurrently, the increased dielectric loss in sample Z6 is likely caused by the elevated glass phase content. Crystalline phases typically show better dielectric properties than their corresponding glassy phases [42]. Specifically, glasses exhibit both a higher dielectric constant and greater dielectric loss compared to their crystalline counterparts. The disordered structure of glass lowers the energy barriers for ionic displacement polarization, enabling easier redistribution of internal charges (polarization) in response to an applied electric field. This results in a higher dielectric constant compared to its crystalline counterpart. Besides, the structural disorder inherent to glasses promotes both intensified relaxation polarization and elevated ionic conductivity.

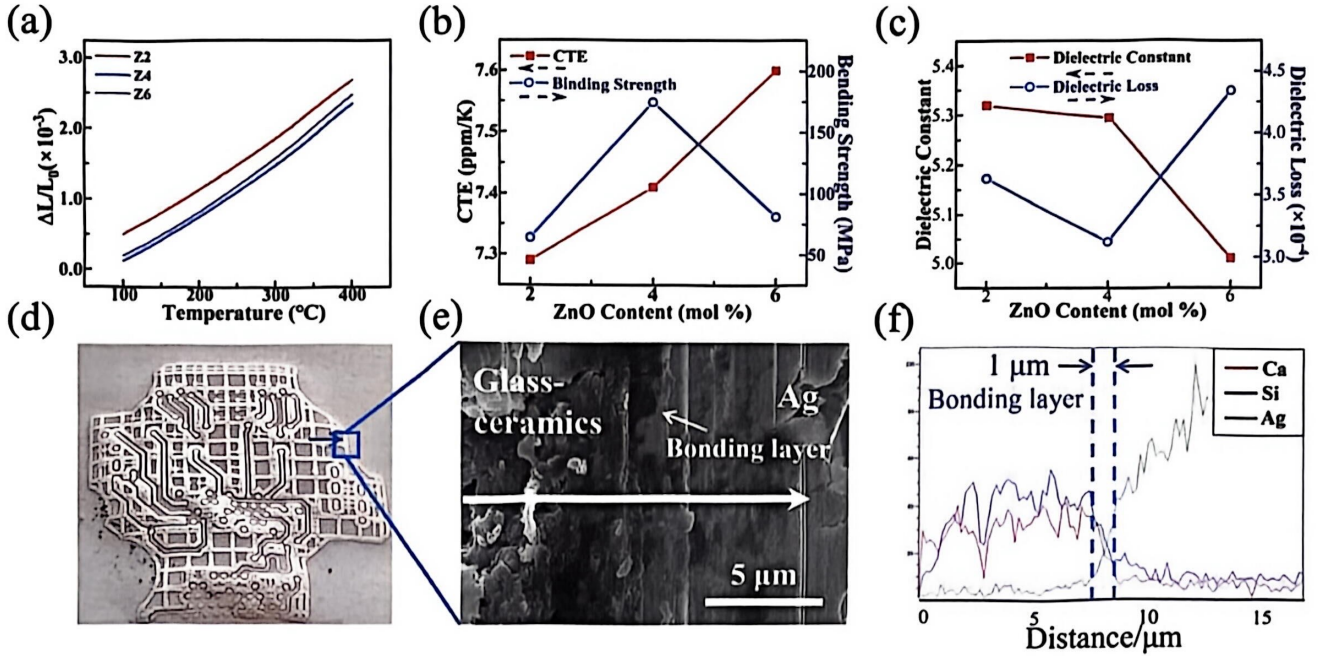

Fig. 4. Characteristics of the ZCBS glass-ceramics. (a) Thermal expansion curve of Z2-Z6 glass-ceramics sintered at 850 °C; (b) Thermal expansion coefficient and bending strength of Z2-Z6 glass-ceramics sintered at 850 °C; (c) Dielectric constant and loss of Z2-Z6 glass-ceramics sintered at 850 °C; (d) Z4 sample cast printed silver circuit after sintering finished appearance; (e) The junction section of the Z4 sample after sintering of the printed silver circuit; (f) Results of EDS line sweep in the arrow direction.

Table 6
Dielectric properties of phases in microcrystalline glass.

	Dielectric constant @1 MHz	Dielectric loss @1 MHz × 10^{-4}	Reference
β-$CaSiO_3$	5.3	2.0	[16]
α-SiO_2	4.0	2.0	[42]

These factors collectively contribute to superior dielectric loss characteristics relative to compositionally equivalent crystalline materials [43]. The dielectric properties of ZCBS glass are presented in Table S3 of the Supplementary Material. It can be observed that the glass phase exhibits less favorable dielectric performance compared to both crystalline phases, aligning with the general trend discussed earlier. Besides, sample Z6 exhibited substantial liquid phase formation during sintering. The low-viscosity liquid migrated toward the bottom region, leaving enlarged intercrystalline voids as evidenced by internal porosity quantification (Fig. S5, Table 5). This increased porosity significantly reduced the dielectric constant due to air inclusion ($\varepsilon_r \approx 1$) while elevating dielectric losses through interfacial polarization mechanisms, which may also serve as a factor influencing variations in the dielectric constant of the samples. Comparative dielectric properties phases in microcrystalline glass were tabulated in Table 6. In general, the introduction of ZnO can increase the liquid phase content, fill the pores, and enhance the sintering and densification of glass-ceramics, aiding the growth of β-$CaSiO_3$ grains and the precipitation of α-SiO_2, thereby improving the dielectric properties of glass-ceramics. However, too much ZnO will produce more glass phase and weaken the dielectric properties, and the interface between large grains and liquid phase is also prone to cracks, thus weakening the bending strength of glass-ceramics. Therefore, the subsequent conduct should inhibit the growth of β-$CaSiO_3$ grains. The performance parameters of Z2-Z6 are summarized in Table 7.

Table 7
Performance parameter of ZCBS glass-ceramics.

Sample	CTE (100 °C-400 °C) ppm/K	Bending strength (MPa)	Dielectric constant @1 MHz	Dielectric loss @1 MHz × 10^{-4}
Z2–850	7.29	63.6	5.32	3.64
Z4–850	7.41	174.3	5.29	3.12
Z6–850	7.60	81	5.01	4.34

3.4. The LTCC device

The Z4 sample with the best performance was cast into a raw porcelain strip, so that the glass powder was evenly distributed on the surface, and the silver circuit was printed on the surface and laminated sintered, as shown in Fig. 4(d). It can be seen that the substrate was still white after co-firing, and there was no obvious yellow Ag diffusion trace. The junction between the co-fired porcelain belt and the silver circuit is enlarged by 15 K times, as shown in Fig. 4(e). It can be seen that there is an obvious bonding layer between the substrate and the silver circuit, and there is no trace of cracking between the two, indicating that the matching of the co-firing is good. In order to study whether Ag is diffused into the substrate, EDS line scanning was carried out at the joint according to the arrow direction of Fig. 4(e). The results are shown in Fig. 4(f). The results show that Ca and Si elements in the substrate have obvious boundaries with Ag elements in the circuit, and the slight overlap can be interpreted as the result of the close combination of the two after sintering, with a length of about 1 μm. Therefore, it can be considered that there is no obvious interaction between Z4 sample and Ag in the sintering process, and there is no trace of Ag diffusion, which proves that the Z4 sample is a LTCC substrate material with application potential.

4. Conclusion

In this study, we explored the effect of Zn^{2+} on the structure of the glass network by changing the ZnO content in the glass, which overcame the challenge that low-boron CBS glass-ceramics are difficult to be sintered at low temperatures. Zn^{2+} exists in the network structure of glass-ceramics as an exosome, which makes the transition from $[BO_4]$ to $[BO_3]$, increasing the amount of NBO, leading to a looser glass network, reducing the thermal stability of the glass, and thus lowering the sintering temperature of glass-ceramics. As ZnO content increases, certain Si-O-Si bonds within the $[SiO_4]$ framework are disrupted, leading to an increased precipitation of α-SiO_2, which contributes to the overall low dielectric constant of the glass-ceramics. Sample Z4 sintered at 850 °C can achieve the highest crystallinity of 89.99 wt %, a bending strength of 174 MPa, a dielectric constant of 5.29, and a dielectric loss of 3.12×10^{-4} at 1 MHz. After co-firing with silver paste, the interface demonstrated good adhesion, with no obvious signs of silver diffusion. Our work proposes a novel optimization approach for advanced glass-ceramics.

Author contributions

The manuscript was written through contributions of all authors. All authors have given approval to the final version of the manuscript.

CRediT authorship contribution statement

Kaiyu Huang: Writing – original draft, Investigation. **Chaofan Wang:** Formal analysis. **Maoyuan Yang:** Software. **Qingchao Jia:** Project administration, Methodology. **Wenzhi Wang:** Writing – review & editing. **Chen Chen:** Visualization. **Huidan Zeng:** Supervision. **Xiongke Luo:** Funding acquisition.

Declaration of competing interest

The authors declare that they have no known competing financial interests or personal relationships that could have appeared to influence the work reported in this paper.

Acknowledgments

The authors are very grateful to the National Natural Science Foundation of China (No. 52272001) and Shanghai Zenfocus Semiconductor Technology Co., Ltd for sample tape casting in this work.

Supplementary materials

Supplementary material associated with this article can be found, in the online version, at doi:10.1016/j.jnoncrysol.2025.123710.

References

[1] Y.-L. Cheng, C.-Y. Lee, W.-J. Hung, G.-S. Chen, J.-S. Fang, Comparison of various low dielectric constant materials, Thin Solid Films 660 (2018) 871–878.
[2] R. Wang, J. Zhou, B. Li, L.T. Li, CaF_2-AlF_3-SiO_2 glass-ceramic with low dielectric constant for LTCC application, J. Alloy Compd. 490 (2010) 204–207.
[3] K. Liu, J. Liang, X. Chen, H. Fu, Microwave dielectric performances of a novel low permittivity $NaCaLa(MoO_4)_3$ ceramic for LTCC applications, J. Mater. Sci: Mater. Electron. 34 (2023) 924–936.
[4] R. Gupta, E.Y. Kim, H.-S. Shin, G.-Y. Lee, D.-H. Yeo, Structural, microstructural, and microwave dielectric properties of $(Al_{1-x}B_x)_2Mo_3O_{12}$ ceramics with low dielectric constant and low dielectric loss for LTCC applications, Ceram. Int. 49 (2023) 22690–22701.
[5] P. Gao, K. Liu, X. Wei, X. Qu, S. Deng, Y. Xiao, J. Yang, Y. Wu, X. Chen, H. Zhou, $NaYW_2O_8$: a novel glass-free microwave dielectric ceramic for LTCC application, Ceram. Int. 49 (2023) 23165–23172.
[6] A. Goulas, G. Chi-Tangyie, D. Wang, S. Zhang, A. Ketharam, B. Vaidhyanathan, I. M. Reaney, D.A. Cadman, W.G. Whittow, J.C. Vardaxoglou, D.S. Engstrøm, Microstructure and microwave dielectric properties of 3D printed low loss $Bi_2Mo_2O_9$ ceramics for LTCC applications, Appl. Mater. Today 21 (2020) 100862.
[7] H. Zuo, X. Tang, H. Zhang, Y. Lai, Y. Jing, H. Su, Low-dielectric-constant $LiAlO_2$ ceramics combined with LBSCA glass for LTCC applications, Ceram. Int. 43 (2017) 8951–8955.
[8] R. Liang, W. Li, X. Zhu, F. Wang, Z. Liu, X. Chen, H. Mao, W. Zhang, Particle size modulation for effectively optimizing the dielectric and mechanical properties of La_2O_3-B_2O_3 based glass-ceramic/ceramic LTCC substrates, Ceram. Int. 49 (2023) 39632–39639.
[9] W. Wang, X. Wang, J. Bao, J. Jiang, Z. Fang, B. Jin, Z. Shi, M.A. Darwish, Y. Chen, Q. Liang, M. Zhang, D. Xu, C. Du, D. Zhou, Low-permittivity $BaCuSi_4O_{10}$-based dielectric ceramics: an available solution to connect low temperature cofired ceramic technology and millimeter-wave communications, Chem. Eng. J. 494 (2024) 153172.
[10] H.-I. Hsiang, S.-W. Yung, C.-C. Wang, Crystallization, densification and dielectric properties of CaO-MgO-Al_2O_3-SiO_2 glass with ZrO_2 as nucleating agent, Mater. Res. Bull. 60 (2014) 730–737.
[11] M.K. Zitani, T. Ebadzadeh, S. Banijamali, R. Riahifar, C. Rüssel, S.K. Abkenar, H. Ren, High quality factor microwave dielectric diopside glass-ceramics for the low temperature co-fired ceramic (LTCC) applications, J. Non-Cryst. Solids 487 (2018) 65–71.
[12] D. Jiang, J. Chen, B. Lu, J. Xi, G. Chen, A new glass–ceramic with low permittivity for LTCC application, J. Mater. Sci: Mater. Electron. 29 (2018) 18426–18431.
[13] C. Dong, H. Wang, T. Yan, J. Zhao, J. Xu, D. Wang, The influence of CaF_2 doping on the sintering behavior and microwave dielectric properties of CaO-B_2O_3-SiO_2 glass-ceramics for LTCC applications, Crystals 13 (2023) 748.
[14] Y. Yu, J. Wang, Y. Yu, Z. Yan, Y. Du, P. Chu, Q. Jing, P. Liu, Synthesis and characterization of single-phase α-cordierite glass-ceramics for LTCC substrates from tuff, Materials 15 (2022) 8758.
[15] H. Wang, Q. Zhang, H. Yang, H. Sun, Synthesis and microwave dielectric properties of $CaSiO_3$ nanopowder by the sol-gel process, Ceram. Int. 34 (2008) 1405–1408.
[16] Q. Jia, R. Yang, L. Zhang, C. Chen, J. Yu, X. Luo, H. Zeng, Weakening the silicate network through six-coordinated magnesium to achieve a high degree of crystallization of β-$CaSiO_3$ in calcium borosilicate glass ceramics for 5G application, Ceram. Int. 50 (2024) 20186–20193.
[17] Q. Jia, W. Wang, H. Zhang, C. Chen, A. Li, C. Chen, H. Yu, L. Zhang, H. Tao, H. Zeng, X. Luo, Y. Yue, Creating single-crystalline β-$CaSiO_3$ for high-performance dielectric packaging substrate, Adv. Mater. 37 (2025) 2414156.
[18] N. Jaziri, A. Boughamoura, J. Müller, B. Mezghani, F. Tounsi, M. Ismail, A comprehensive review of thermoelectric generators: technologies and common applications, Energy Rep. 6 (2020) 264–287.
[19] D. He, H. Zhong, C. Gao, Effect of TiO_2 doping on crystallization, microstructure and dielectric properties of CBS glass-ceramics, J. Alloy. Compd. 799 (2019) 50–58.
[20] S.-F. Wang, B.-C. Lai, Y.-F. Hsu, C.-A. Lu, Dielectric properties of CaO-B_2O_3-SiO_2 glass-ceramic systems in the millimeter-wave frequency range of 20–60 GHz, Ceram. Int. 47 (2021) 22627–22635.
[21] Y. Zhao, Q. Zhang, J. Chen, Y. Yi, M. Zhou, J. Cui, Effects of B_2O_3 content on crystallization behavior and properties of low temperature co-fired CaO-B_2O_3-SiO_2 glass-ceramics, J. Mater. Sci: Mater. Electron. 35 (2024) 225.
[22] D. He, C. Gao, Effect of boron on crystallization, microstructure and dielectric properties of CBS glass-ceramics, Ceram. Int. 44 (2018) 16246–16255.
[23] R. Yang, Q. Jia, L. Zhang, C. Chen, J. Yu, H. Zeng, X. Luo, Unveiling the effect of phase separation on crystallization of calcium borosilicate glass-ceramics, Ceram. Int. 50 (2024) 11003–11011.
[24] Y. Fu, P. Li, H. Tao, L. Zhang, M. Xin, Y. Chang, Y. Xia, H. Zhou, The effects of Ca/Si ratio and B_2O_3 content on the dielectric properties of the CaO-B_2O_3-SiO_2 glass–ceramics, J. Mater. Sci: Mater. Electron. 30 (2019) 14053–14060.
[25] J. Xi, B. Lu, J. Chen, G. Chen, F. Shang, J. Xu, C. Zhou, C. Yuan, Ultralow sintering temperature and permittivity with excellent thermal stability in novel borate glass-ceramics, J. Non-Cryst. Solids 521 (2019) 119527.
[26] P. Zhang, Z. Chen, B. Li, Effect of BaO on crystallization, sintering, and properties of MgO-Al_2O_3-SiO_2 glass–ceramics, J. Mater. Sci: Mater. Electron. 33 (2022) 2846–2854.
[27] Q. Xia, C.-W. Zhong, J. Luo, Low temperature sintering and characteristics of K_2O-B_2O_3-SiO_2-Al_2O_3 glass/ceramic composites for LTCC applications, J. Mater. Sci: Mater. Electron. 25 (2014) 4187–4192.
[28] L. Chen, J. Xie, M. Wang, S. Cao, X. Cui, X. Liang, J. Zhang, J. Han, H.U. Kaiwen, Na_2O/Li_2O ratio dependency on the thermal, mechanical, dielectric properties and chemical stabilities of Li_2O-Al_2O_3-SiO_2 glass, J. Wuhan Univ. Technol. 37 (2023) 1129–1136.
[29] L. Song, J. Wu, Z. Li, X. Hao, Y. Yu, Crystallization mechanisms and properties of α-betacordierite glass–ceramics from K_2O-MgO-Al_2O_3-SiO_2 glasses, J. Non-Cryst. Solids 419 (2015) 16–26.
[30] Z. Qing, B. Li, Y. Li, H. Li, S. Zhang, Microstructure and properties of ZnO doped Li_2O-Al_2O_3-SiO_2 glass-ceramic for LTCC applications, J. Mater. Sci: Mater. Electron. 27 (2015) 1597–1601.
[31] C.Y. Ng, T.P. Chen, L. Ding, Y. Liu, M.S. Tse, S. Fung, Z.L. Dong, Static dielectric constant of isolated silicon nanocrystals embedded in a SiO_2 thin film, Appl. Phys. Lett. 88 (2006) 063103.
[32] C.S. Lee, K.A. Matori, S.Hj.A. Aziz, H.M. Kamari, I. Ismail, M.H.M. Zaid, Influence of zinc oxide on the physical, structural and optical band gap of zinc silicate glass system from waste rice husk ash, Optik (Stuttg) 136 (2017) 129–135.
[33] S. Das, A. Madheshiya, M. Ghosh, K.K. Dey, S.S. Gautam, J. Singh, R. Mishra, C. Gautam, Structural, optical, and nuclear magnetic resonance studies of V_2O_5-doped lead calcium titanate borosilicate glasses, J. Phys. Chem. Solids 126 (2019) 17–26.

[34] F.F. Al-Harbi, N.S. Prabhu, M.I. Sayyed, A.H. Almuqrin, A. Kumar, S.D. Kamath, Evaluation of structural and gamma ray shielding competence of Li_2O-K_2O-B_2O_3-HMO (HMO = SrO/TeO_2/PbO/Bi_2O_3) glass system, Optik (Stuttg) 248 (2021) 168074.
[35] A.V.S. Yeswanth, L.S. Deo, A.S.Rao Anu, G.V. Prakash, Down-conversion and up-conversion photoluminescence studies of Er^{3+} doped calcium zinc borosilicate glass for optical fiber amplifiers, J. Non-Cryst. Solids 609 (2023) 122280.
[36] M.A. Azooz, H.A. Elbatal, Preparation and characterization of invert ZnO-B_2O_3 glasses and its shielding behavior towards gamma irradiation, Mater. Chem. Phys. 240 (2020) 122129.
[37] W. Gao, S. Cao, L. Li, J. Wang, C. Liu, J. Han, Network structure, crystallization behavior, and microwave dielectric properties of ZnO-B_2O_3 glass-ceramics with ZrO_2 additions, J. Alloy. Comp. 953 (2023) 170145.
[38] Y. Pi, W. Zhang, Y. Zhang, W. Zou, Z. Zhang, F. Wu, Migration and transformation of heavy metals in glass-ceramics and the mechanism of stabilization, Ceram. Int. 47 (2021) 24663–24674.
[39] W. Gao, J. Zhang, S. Cao, J. Wang, L. Li, J. Ruan, J. Han, Sintering behavior, structure and dielectric properties of CuO-ZnO-MgO-B_2O_3 glass-ceramics for ULTCC applications, J. Eur. Ceram. Soc. 42 (2022) 4987–4997.
[40] G.S. Macena, A.S. Abyzov, V.M. Fokin, E.D. Zanotto, E.B. Ferreira, Off-stoichiometry effects on crystal nucleation and growth kinetics in soda-lime-silicate glasses. The combeite ($Na_2O{\bullet}2CaO{\bullet}3SiO_2$) – devitrite ($Na_2O{\bullet}3CaO{\bullet}6SiO_2$) joint, Acta Mater. 196 (2020) 191–199.
[41] T. Yan, W. Zhang, H. Mao, X. Chen, S. Bai, The effect of CaO/SiO_2 and B_2O_3 on the sintering contraction behaviors of CaO-B_2O_3-SiO_2 glass-ceramics, Int. J. Mod. Phys. B 33 (2019) 1950070.
[42] H. Yu, J. Liu, M. Zeng, Structure and dielectric properties of zinc borate glass-ceramics modified by magnesium, J Mater. Sci: Mater. Electron. 27 (2016) 7109–7114.
[43] J.-M. Wu, H.-L. Huang, Microwave properties of zinc, barium and lead borosilicate glasses, J. Non-Cryst. Solids 260 (1999) 116–124.